Non-intrusive temperature measurements for transient freezing in laminar internal flow using laser induced fluorescence

Kaaks, Bouke Johannes; Couweleers, Sebastian; Lathouwers, Danny; Kloosterman, Jan Leen; Rohde, Martin

DOI
10.1016/j.expthermflusci.2024.111184

Publication date
2024

Document Version
Final published version

Published in
Experimental Thermal and Fluid Science

Citation (APA)
Kaaks, B. J., Couweleers, S., Lathouwers, D., Kloosterman, J. L., & Rohde, M. (2024). Non-intrusive temperature measurements for transient freezing in laminar internal flow using laser induced fluorescence. *Experimental Thermal and Fluid Science*, *155*, Article 111184. https://doi.org/10.1016/j.expthermflusci.2024.111184

Experimental Thermal and Fluid Science 155 (2024) 111184

Contents lists available at ScienceDirect

Experimental Thermal and Fluid Science

journal homepage: www.elsevier.com/locate/etfs

Non-intrusive temperature measurements for transient freezing in laminar internal flow using laser induced fluorescence

Bouke Johannes Kaaks *, Sebastian Couweleers, Danny Lathouwers, Jan-Leen Kloosterman, Martin Rohde

Delft University of Technology, Department of Radiation Science and Technology, Mekelweg 15, 2629 JB, Delft, Netherlands

ARTICLE INFO

Dataset link: Experimental dataset referring to: Non-intrusive temperature measurements for transient freezing in laminar internal flow using laser induced fluorescence (Original data)

Keywords:
Transient freezing
Laminar internal flow
Non-intrusive temperature measurements
Laser Induced Fluorescence

ABSTRACT

This work presents two color LIF temperature measurements for the transient freezing in a square channel under laminar flow conditions. This is the first time non-intrusive temperature measurements were performed within the thermal boundary layer during the transient growth of an ice layer in internal flow. A combination of a local outlier factor algorithm and a smoothing operation was used to remove the top to bottom striations and reduce the other measurement noise. The temperature uncertainty in our measurements was between $\sigma = 0.3$ °C and $\sigma = 0.5$ °C. For the largest temperature difference between the bulk and the melting point of 14.6 °C, good results were obtained. As such, the current campaign demonstrates the potential of LIF as a non-intrusive temperature measurement technique for solid–liquid phase change experiments. However, some artefacts were present within the vicinity of the ice-layer due to the scattering of the laser light, especially near the inlet of the channel where the ice-layer is curved instead of flat. LIF measurements taken within a short time span prior to the onset of ice freezing showed approximately 2 °C of subcooling, consistent with previous findings. In addition, an anomalous behavior within the thermal boundary layer was observed, with a much smaller temperature gradient within the first few mm above the cold plate and a point of inflection in the temperature profile. The anomalous temperature behavior is possibly attributed to enhanced natural convection as a result of the subcooling at the cold plate surface.

1. Introduction

Over the last decades, solid–liquid phase change has been an active field of research, due to its relevance for numerous industrial applications (amongst which metallurgy [1–3], latent heat storage [4,5] and the Molten Salt Reactor [6,7]) and the highly complex coupling between the non-linear heat transfer (including rapidly changing thermophysical properties) and the surrounding flow-field. Earlier experimental campaigns relied on intrusive techniques such as the pour-out method for identifying the solid–liquid interface and thermocouples for measuring the temperature [1]. However, these methods are invasive and may disturb the melting process [3].

It is therefore recommended to use non-intrusive techniques when conducting solid–liquid phase change experiments, especially when the purpose is to generate experimental data suitable for numerical model validation. Indeed, more recent experimental campaigns used photographic observations [8–10], X-ray diffraction [2], or the shadowgraph technique [4] for tracing the solid–liquid interface position. In addition, recent efforts were made to measure the velocity field using particle image velocimetry (PIV) [4,5,11–13] or ultra-sound doppler velocimetry [3].

On the other hand, very few non-intrusive temperature measurements have been performed for solid–liquid phase change experiments. Even in recent experimental campaigns (for instance those of Ben David et al. [3] and Vogel et al. [4]), thermocouples were used for measuring the temperature distributions in the solid and the liquid fields. However, it has been shown that the use of thermocouples leads to a distorted flow-field within the liquid phase and can considerably alter the melting and freezing-process [5,14]. A few examples in literature report the use of an alternative, non-intrusive approach for measuring the temperature distributions. Kowalewski et al. [11] measured the temperature during the freezing of water using thermochromic liquid crystal (TLC) particles [11]. Chen et al. measured the temperature distribution in a melting paraffin wax (with embedded aluminum foam) using an infrared camera [15]. Kumar et al. measured the temperature fields during the freezing of water based on the temperature dependency of the refractive index, using Mach–Zehnder interferometry [16].

* Corresponding author.
E-mail addresses: b.j.kaaks@tudelft.nl (B.J. Kaaks), m.rohde@tudelft.nl (M. Rohde).

https://doi.org/10.1016/j.expthermflusci.2024.111184
Received 10 November 2023; Received in revised form 11 February 2024; Accepted 10 March 2024
Available online 11 March 2024

Nomenclature

Acronyms

FOV	Field of View
LIF	Laser Induced Fluorescence
PIV	Particle Image Velocimetry
ROR	Region Of Reference

Dimensions

d	diameter (m)
D_h	hydraulic diameter (m)
H, W, L	height, width, length (m)
x, y, z	cartesian coordinate system (m)

Physical quantity

λ	wave length (nm)
ϕ	flow rate ($\mathrm{L\,s^{-1}}$)
C	concentration $\mathrm{kg\,m^{-3}}$
f	frequency (Hz)
I	fluorescent energy per unit volume ($\mathrm{W\,m^{-3}}$)
t	time (s, min or h)
T	temperature (°C

Thermophysical property

α	thermal diffusivity ($\mathrm{m^2\,s^{-1}}$)
β	thermal expansion coefficient ($\mathrm{K^{-1}}$)
μ	dynamic viscosity (Pa s)
ρ	density ($\mathrm{kg\,m^{-3}}$)
c_p	specific heat ($\mathrm{J\,kg^{-1}\,K^{-1}}$)
k	thermal conductivity ($\mathrm{W\,m^{-1}\,K}$)
L	latent heat of fusion ($\mathrm{kJ\,kg^{-1}}$)

Fluorescence

ϵ	fluorescence re-adsorption correction coefficient
ϕ	quantum efficiency of the dye
I_0	incident light flux ($\mathrm{W\,m^{-2}}$)

Optics

f	focal length of the camera
M_0	magnification factor
Z_0	image distance from the center of the lens to the image plane
z_0	object distance to the effective center of the lens

Dimensionless numbers

$Pr = \frac{\mu c_p}{k}$	Prandtl number
$Re = \frac{\rho u D_h}{\mu}$	Reynolds number

Other symbols

σ	uncertainty
C_F	correction factor
G	image intensity

Subscript

α	corresponding to the temperature sensitive dye
β	corresponding to the reference dye
c	of the cold plate
R	corresponding to the ratio between the two dyes
in,set	of the inlet set-point
in	of the inlet
$stat$	statistical
sys	systematic

Gong et al. [17] measured the temperature distribution of melting n-octadecane using laser induced fluorescence (LIF).

LIF uses temperature sensitive dyes excited by laser light to measure the temperature field [18]. So far, LIF temperature measurements have been performed for a variety of cases, such as a heated jet [19,20], a buoyant plume [21,22], natural convection flow in a cavity [23], temperature measurements of evaporating and combusting droplets [24], an impinging jet [25–27], Rayleigh–Bènard convection [28] and the temperature distribution in the wake of a heated cylinder [29]. Furthermore, LIF has been used to identify the gas–liquid interfaces in multiphase flow [30] and to measure the ice fraction in supercooled water droplets [31]. Compared to TLC, LIF has a better range. However, the accuracy of LIF is largely dependent on the intensity resolution [22]. For instance, Coolen et al. achieved an accuracy of ±1.7 °C over a temperature range of 19.8–55.2 °C and using an 8 bit camera whilst Funatani et al. reported an uncertainty of ±0.3 °C using a color CCD camera with 10 bits for each RGB, and a temperature range of 30.0–60.0 °C.

The main purpose of this paper is to demonstrate the potential and limitations of LIF as a non-intrusive technique for measuring the temperature distribution in the liquid phase during solid–liquid phase change experiments. To this end, we present two-color LIF temperature measurements of the water above the ice–water interface during the transient freezing of ice in a square channel under laminar flow conditions. Compared to the work by Gong et al., several improvements were incorporated. These are the use of a two color (instead of a one color) LIF technique, the use of a post-processing algorithm to remove striations and other artefacts, and a detailed analysis of the uncertainty in the measured temperature fields. So far, the experimental data available for the transient growth of an ice-layer in internal flow is limited to three investigations only [12,13,32]. This is the first time non-intrusive temperature measurements were performed above an evolving solid–liquid interface in internal flow.

Additional temperature measurements were performed in the minutes prior to the onset of freezing. In our previous PIV campaign [33], the onset of freezing was marked by a sudden increase of the cold plate temperature, accompanied by a rapid spreading of the ice over the cold plate. A similar behavior of the cold-plate was observed by Savino et al. [32], who collected evidence of sub-cooling by performing thermocouple measurements within the thermal boundary layer in the time span from before the ice formed until after the thermocouple became embedded in the ice layer. The present work is the first to confirm the presence of subcooling within the thermal boundary layer of a flowing liquid through non-intrusive temperature measurements.

The structure of this paper is as follows: in Section 2 we describe the experimental method, including the design of the experimental measurements, the basic principle behind the LIF measurements, the optical setup, the experimental procedure, the image postprocessing, the temperature calibration and the uncertainty quantification. In Section 3 we show our results and discussion, including temperature measurements taken both near the inlet and at the center of the channel for four different inlet temperatures, and temperature measurements taken during the ‘lag time’ prior to the onset of freezing. Finally, we present our conclusion and recommendations for future work in Section 4.

2. Experimental methodology

2.1. Design of the ESPRESSO facility

The ESPRESSO (Experiment for Re-Melting and Salt Solidification) facility consists of a water tunnel with a square channel test-section ($H \times W \times L = 5.00 \pm 0.03\,\text{cm} \times 5.00 \pm 0.03\,\text{cm} \times 145.0 \pm 0.1\,\text{cm}$), made of poly (methyl methacrylate) (PMMA) in order to guarantee optical access. The side walls of the test section have a thickness of $d = 5.0 \pm 0.1\,\text{mm}$ and the removable top lid has a thickness of $d = 2.00 \pm 0.02\,\text{cm}$. The growth of the ice layer is initiated from an aluminum cold plate (offset fin configuration) at the bottom of the test section ($H = 2.10 \pm 0.02\,\text{cm}, L = 148.5 \pm 0.1\,\text{cm}, W = 9.50 \pm 0.03\,\text{cm}$). The cold plate is coupled to a Julabo FL1701 recirculating cooler, using the ethylene–glycol based Thermal-G as a refrigerant at a maximum flow rate of $\phi_v = 23.0\,\text{L}\,\text{min}^{-1}$. Hence, the cold-plate is capable of reaching a minimum temperature of $T_c = -20.0\,°\text{C}$. To impose a uniform inlet velocity profile at the entrance of the test section, the upstream section features a combination of a diffuser, settling chamber and a converging nozzle. The water is stored in a buffer vessel of approximately 100 L in volume and recirculated through the test section by a pump with an electronic frequency drive, capable of reaching a maximum flow rate of $\phi_v = 1.4\,\text{L}\,\text{s}^{-1}$. To remove the (large) air bubbles introduced by the pump, the flow is passed through a bubble column. The inlet is pre-cooled using a brazed plate liquid heat exchanger (SWEP, Sweden), located after the pump and coupled to a second Julabo FL1701 recirculating cooler, which uses cold water as the refrigerant. The temperatures in the cold-plate are measured through a series of 8 thermocouples with an accuracy of $\pm 0.2\,°\text{C}$, equally distributed along the length of the cold plate at a spacing of 20.5 cm. In addition, the temperatures of the buffel vessel as well as the bulk inlet and outlet temperatures are also recorded using K-type thermocouples. The flow rate is recorded using a Proline Promag 10 W magnetic flow metre (Endress Hausser, Germany) with an accuracy of $\sigma_{\phi_v} = \pm 0.5\%$ or $\sigma_u = \pm 2\,\text{mm}\,\text{s}^{-1}$ for flow-rates outside the official measurement range. A graphical representation of the ESPRESSO (Experiment for Re-Melting and Salt Solidification) facility is given in Fig. 1. For a more comprehensive overview of the design of the experimental facility, see Kaaks et al. [13].

2.2. Laser induced fluorescence: principle

Laser induced fluorescence uses temperature-sensitive fluorescent dyes as a whole-field temperature diagnostic. Upon excitation through exposure to laser light, the dyes emit light at a certain wave-length, of which the intensity can be used to determine the temperature. Neglecting Beer's attenuation of the incident laser light, the fluorescent energy I ($\text{W}\,\text{m}^{-3}$) emitted per unit volume is defined as:

$$I = I_0 C \phi \epsilon \tag{1}$$

where I_0 is the incident light flux ($\text{W}\,\text{m}^{-2}$), ϕ is the quantum efficiency of the dye (i.e. ratio of the total energy emitted per quantum of energy absorbed), C is the concentration of the dye solution ($\text{kg}\,\text{m}^{-3}$) and ϵ ($\text{m}^2\,\text{kg}^{-1}$) is a coefficient to correct for the fluorescence re-adsorption [18]. When recording camera images, the image intensity G is proportional to the fluorescence intensity [27]:

$$G = \alpha I + G_{noise} \tag{2}$$

where α is an optical transfer function and G_{noise} is the camera offset noise.

For some organic dyes, the quantum efficiency is dependent on the temperature, resulting in a temperature sensitive fluorescent intensity. Thus, if one can keep the incident light flux I_0 and the concentration constant, one can measure the temperature (on the other hand, when keeping the incident light flux and the temperature constant, one can measure the concentration, see for instant Hjertager et al. [34]).

In practice, I_0 is affected by a variety of factors, such as convergence and divergence of the light sheet, refraction of the light sheet (for instance due to gradients in the refractive index as a result of the temperature differences), variation in incident laser intensity (in particular for setups using a pulsed laser), and scattering of the laser light due to air bubbles or other particles blocking the laser transmission and the transient growth of the ice-layer.

For (quasi) steady-state experiments, a careful normalization is performed using a series of reference images taken at a known uniform temperature field to correct for the spatial distribution of the laser sheet intensity. In addition, by recording the energy of the laser, the pulse-to-pulse energy of the laser can be taken into account [22,29]. However, it is difficult to eliminate the effect of the laser light reflection due to the transient growth of the ice layer using these techniques. In addition, the transient freezing process possibly affects the dye concentration.

Instead, a temperature-insensitive reference dye can be used as a means of measuring the local, instantaneous intensity of the laser sheet [18]. This leads to the use of a mixture of two different dyes, one temperature sensitive and one temperature insensitive, with different emission spectra. Assuming the emission spectra can be perfectly separated using a combination of beam-splitting optics and band-pass filters, and neglecting the offset noise, the ratio between the two dyes is written as:

$$\frac{G_\alpha}{G_\beta} = \frac{I_\alpha}{I_\beta} = \frac{C_\alpha \phi_\alpha \epsilon_\alpha}{C_\beta \phi_\beta \epsilon_\beta} \tag{3}$$

where the subscript α and β refer to the temperature-sensitive dye and the reference dye respectively. In theory, the intensity ratio is now independent of the incident light flux I_0, whilst still dependent on the temperature [18,26]. In practice, there is some overlap between the emission spectrum of the two fluorescent dyes, resulting in an imperfect separation of the spectra. Consequently, some fraction of I_α is detected by camera β and vice versa. This can be accounted for by a proper calibration procedure [18,26].

2.3. Selection of the fluorescent dyes

Rhodamine B (RhB) was selected as the temperature-sensitive dye, due to its high temperature sensitivity (2.3% K^{-1}) and because its absorption spectrum covers the range of 470–600 nm, making excitation easy by conventional lasers [18]. Rhodamine 110 has a similarly suitable adsorption spectrum, but has a very low temperature sensitivity and was thus selected as the reference dye. The dye concentrations were optimized in order to achieve a good signal output in both camera feeds. The procedure involved adding droplets of a concentrated solution of each dye to the buffer vessel, until the maximum intensity of camera α (i.e. for RhB) reached half the dynamic range at 20 °C (leaving room for intensity changes due to a change in temperature) and the maximum intensity of camera β (i.e. for Rh110) was close to the maximum dynamic range. Due to the procedure and the large volume of fluid involved, it was difficult to quantify the exact concentration of the dyes, but the range falls within 10 to 100 $\mu\text{g}\,\text{L}^{-1}$. The basic properties of the fluorescent dyes used are given in Table 1.

2.4. Optical setup

The dissolved dyes were excited using a class-IV, 5 W shuttered continuous wave laser (diode pumped, solid-state) with a wave length of $\lambda = 532$ nm (LaVision, Germany). A laser guiding arm (LaVision, Germany) was used to introduce the laser sheet from the top of the test section and a combination of a spherical and a cylindrical lens was used to generate the laser sheet. The sheet has a beam waist thickness of approximately 1 mm. The region of interest is observed simultaneously by two CMOS cameras (Imager MX-4M, LaVision, Germany) with 12 bit of dynamic range and 4 MP of resolution (2008 × 2086 pixels, pixel size of 5.5 μm × 5.5 μm). The field of view (FOV) was $[\Delta x, \Delta y] = 8.03\,\text{cm} \times$

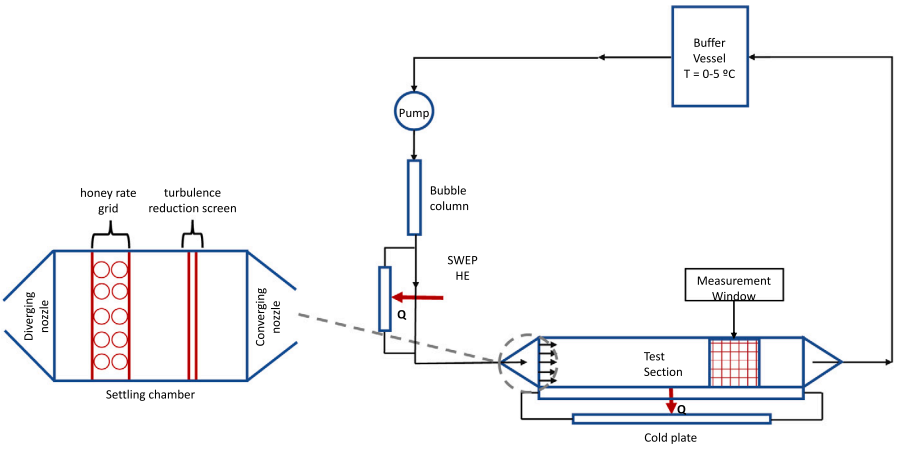

(a) Sketch of ESPRESSO Experimental Facility.

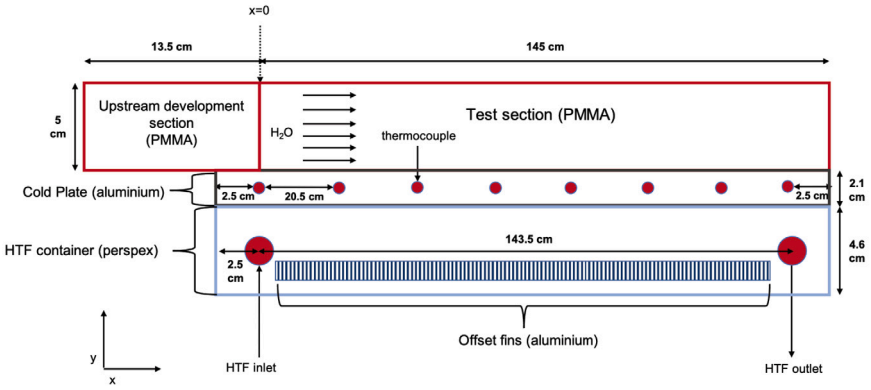

(b) Zoom in of test section (side view).

Fig. 1. Graphical representation of ESPRESSO experimental facility. Here, PMMA stands for poly(methyl methacrylate), HE stands for heat exchanger and HTF stands for heat transfer fluid.

Table 1
Basic characteristics of RhB and Rh110 dissolved in deionized water (T = 20 °C) [18].

Dye	Molecular weight	λ_{abs} [nm]	λ_{em} [nm]	ϕ	Temperature sensitivity [K^{-1}]
Rhb	479.02	554	575	0.31	2.3%
Rh110	366.8	496	520	0.8	0.13%

8.34 cm. This translates to a spatial resolution of 40 μm per pixel for both the x- and the y-direction. The spatial resolution can also be determined by estimating the magnification factor:

$$M_0 = \frac{Z_0}{z_0}, \tag{4}$$

where Z_0 is the image distance from the center of the lens to the image plane and z_0 is the object distance to the effective center of the lens. The total distance from the camera's to the center of the perspex channel is approximately 40 cm (including the distance from the camera's to the beamsplitter, the distance from the beam splitter to the perspex channel wall and the half-width of the channel). Z_0 is estimated applying the Gauss lens law

$$\frac{1}{Z_0} + \frac{1}{z_0} = \frac{1}{f}, \tag{5}$$

where f is the focal length of the camera (i.e. 50 mm), resulting in a magnification factor of approximately $M_0 = 0.14$. Dividing the original pixel size by the magnification factor yields a similar spatial resolution of approximately 40 μm per pixel for both the x- and the y-direction.

Both cameras mount an AF-S 50 mm F/1.4 (Nikon) lens. A first separation of the two spectral bands is achieved using a dichroic beamsplitter (ZT561rdc-UF3 of Chroma, USA) and a second separation is achieved using interference filters at 600 nm and 550 nm respectively, both with a full width half maximum (FWHM) of 20 nm. To limit the reflection of the laser, black aluminum tape was applied to the surface of the cold wall and the back wall of the test section. A schematic of the optical setup is shown in Fig. 2.

Prior to the start of the experimental campaign, an image calibration procedure is performed using a calibration plate. A 3rd order polynomial function was fitted by the least-squares method in order to transform the image coordinate to the physical coordinate. An additional self calibration step is performed to correct for possible errors due to light sheet or calibration plate misalignment. The root mean square errors of the image calibration are 1.1 pixel and 1.6 pixel for camera α and β respectively.

2.5. Experimental procedure

The temperature fields were measured for four different set point temperatures of the inlet temperature (i.e. $T_{in,set}$ = 15 °C, $T_{in,set}$ = 10 °C, $T_{in,set}$ = 5 °C and $T_{in,set}$ = 0.5 °C). The flow-rate corresponds to $Re = 474$ and the set point of the cold plate is set to $T_{c,set} = -10$ °C. Measurements were performed at both the inlet and at the center of the test section. The experiment was initialized as follows. First the water was recirculated at the maximum available flow rate whilst the cold plate and the inlet were being cooled according to the desired set-point

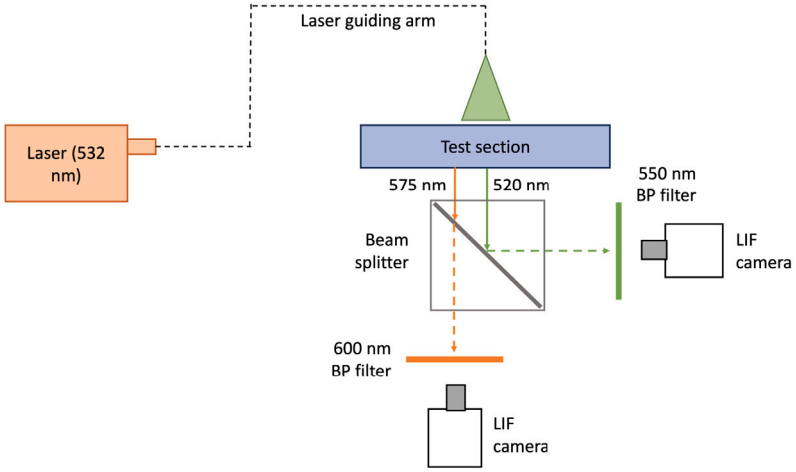

Fig. 2. Optical setup of LIF experiments.

temperatures. After the cold plate and the inlet temperatures stabilized, the flow rate was reduced to the desired value. Because the cold plate was in direct contact with the water flow above, reducing the flow rate of the water (and therefore the heat exchange between the water and the surface of the cold-plate) resulted in a further decrease of the cold plate temperature. The onset of freezing was marked by a sudden sharp increase of the cold plate temperature, and was therefore used to determine $t = 0$ in our experiments (seeKaaks et al. 2023 [13]).

During the first hour after the onset of ice-formation at $t = 0$, an image recording was made every 5 min. At each measurement, 25 pairs of images were recorded with a frequency of $f_{sample} = 10$ Hz. and a laser pulse duration of $t_{pulse} = 8500$ µs. The camera and laser were synchronized using a programmable timing unit (PTU, LaViSion, Germany) operated using Davis v8 software. During the second hour of the experiment, this frequency was reduced to each 15 min and after the third hour to 30 min. During the experiment, the temperatures measured by the thermocouples as well as the flow rate were recorded in real time and stored using the LabView software.

2.6. Post-processing of images

The images are pre-processed using the LaVision 8 software. First, an average of 100 camera dark images (taken with the lens cap on) is subtracted from the LIF images of camera α and camera β in order to remove the dark current noise from the images. Next, a white image correction is performed. Here, the white image is the average of 25 images of the area of interest taken at an uniform reference temperature of $T_{ref} = 17.8 \pm 0.2$ °C. The whole preprocessing operation is described as:

$$\tilde{I}_{\alpha,\beta}(x,y) = \frac{\left(I_{\alpha,\beta}(x,y) - I_{dark_{\alpha,\beta}}(x,y)\right)}{I_{WI_{\alpha,\beta}}(x,y)} \overline{I}_{WI_{\alpha,\beta}} \tag{6}$$

Here, $\overline{I}_{WI_{\alpha,\beta}}$ is the spatial average of the white image in the area of interest.

The corrected image intensities from camera α and camera β are subsequently divided by one another to obtain the ratio used as a basis for the temperature calculations:

$$I_R = \frac{\tilde{I}_\alpha}{\tilde{I}_\beta}, \tag{7}$$

where I_R is used as the symbol for the ratio between the image intensities.

Finally, the average intensity ratio of each sample set (containing 25 images from both camera's α and β) is calculated. An example of the intensity ratio map is shown in Fig. 3(a) for the center of the channel and Fig. 4(a) for the inlet of the channel. Here, $y = 0$ denotes the bottom of the test section where the cold-plate is located and $x = 0$ denotes the center of the area of interest.

The intensity ratio map is significantly contaminated by the presence of multiple top-bottom striations running through the area of interest. These striations are caused by the refraction of the laser light due to factors such as the fluid's irregular density, air bubbles,[1] or inhomogeneities in the top lid of the test section where the laser enters (caused by dirt particles, fat stains or surface damage). Due to the use of the two-color LIF technique, these striations were expected to be canceled out. However, as shown by Sakibara et al. [28], a mismatch in the intensity profiles between the images of cameras α and β can prevent the elimination of the striations, leading to a significant error in the intensity ratio (and thus the temperature). This mismatch can be caused by small errors in the image calibration (as shown in the previous section), a different focusing and aberrations of the object lenses, or from astigmatic aberration caused by the inclined beam splitter.

In previous work, striations were corrected using a correction map based on a reference region with a uniform temperature (and therefore uniform intensity) [22,27,29], or using a transfer function in the Fourier domain in order to achieve perfect overlap between the intensity profiles of the α and β camera images [28]. In the present work, a different approach was adopted and the top to bottom striations were consider to be outliers. The outliers were removed by scanning the intensity ratio map from top to bottom and using a local outlier factor (LOF) algorithm [35]. The LOF algorithm assigns a degree of being an outlier to each data point, depending on how isolated the data point is with respect to its neighbors. As such, the LOF algorithm differs from other outlier removal algorithms which consider being an outlier as a binary property. The LOF of each sample point is calculated according to a density-based clustering algorithm, where the density is calculated according to the assigned number of neighbors (500 for the center of the channel based on a very small temperature gradient in the x-direction and 200 for the inlet of the channel, where the temperature gradient in the x-direction is more significant) and the distance from the data point to each neighbor. The thresholds for the LOF are determined based on a user-defined degree of contamination (here, 0.5 was used for the center of the channel and 0.33 for the inlet of the channel). These thresholds correspond to the high noise level observed in our measurements as a result of the top to bottom striations. Data points for which the LOF exceeds the threshold are replaced by a linear interpolation.

[1] Especially small air bubbles may pass through the bubble trap.

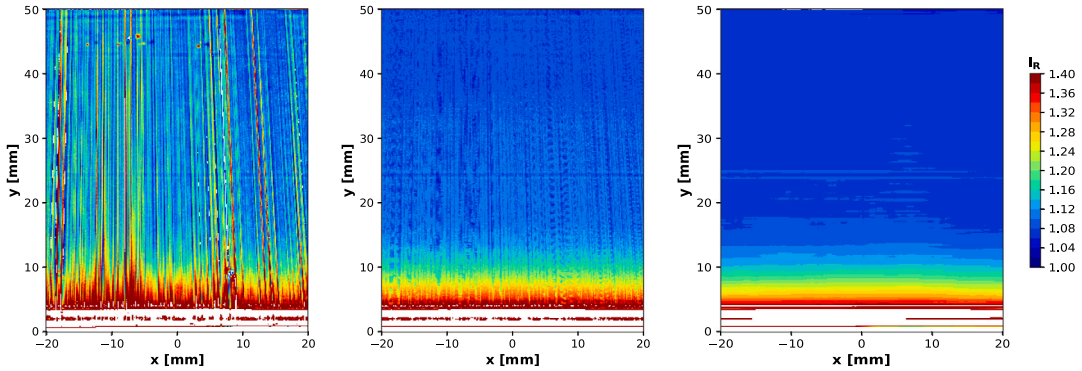

(a) Intensity ratio map after pre-processing.

(b) Intensity ratio map after striation removal through LOF algorithm.

(c) Intensity ratio map after smoothing.

Fig. 3. Intensity ratio map after the different postprocessing steps (pre-processing (a), striation removal (b), smoothing (c)), taken at the center of the test-section for $t = 5$ min after the onset of ice-formation. The experimental settings were: $Re \approx 474$, $T_{in,set} = 15$ °C and $T_{c,set} = -10$ °C.

Consistent with the thresholds chosen, 49.6% of the data points in Fig. 3(a) and 32.4% of the data points in Fig. 4(a) were considered outliers and were replaced by a linear interpolation. The resulting 'cleaned' intensity ratio maps are shown in Figs. 3(c) and 4(c). Whilst the top to bottom striations were successfully removed using the outlier removal procedure and a large reduction in overall noise levels was obtained, the information content of our measurements was reduced significantly (by respectively 49.6% and 32.4%) as a consequence. Please note that the outliers were removed by only considering the intensity ratio variation in the x-direction, and the gradients in the y-direction were therefore preserved. For this reason, and considering the high noise level in the raw intensity ratio maps, we consider the chosen approach to be justified. For future work, we recommend improving the quality of the experimental setup in order to obtain raw intensity ratio maps with a lower noise level (see Section 3 for some suggestions).

Finally, the remaining image noise was reduced by smoothing the image using a moving average window. For the center of the channel (between $x = 70$ cm and $x = 80$ cm), a smoothing window of $N_x \times N_y = 200 \times 5$ pixels was used reducing the overall spatial resolution to 8 mm in the x-direction and 0.2 mm in the y-direction. The large degree of smoothing in the x-direction (resulting in 10 collapsed data points within the FOV) for the center of the channel was justified, because the temperature variation in this direction is very small as a result of the flow being (almost) fully developed. For the inlet of the channel, a smoothing window of $N_x \times N_y = 20 \times 5$ pixels was used reducing the overall spatial resolution to 0.8 mm in the x-direction and 0.2 mm in the y-direction. Here, there is a more significant temperature gradient in the x-direction due to the development of the thermal boundary layer. The chosen window sizes were believed to be a good compromise between achieving sufficient spatial resolution and reducing the image noise. The smoothed intensity ratio maps are shown in Fig. 3(c) for the center of the channel and Fig. 4(c) for the inlet of the channel. For Figs. 4(a) and 4(c), artefacts were observed near the top of the channel at $y = 50$ mm. This was attributed to reflections of the laser light from the top lid, resulting in noisy measurements near the top of the channel.

2.7. Temperature calibration procedure

The temperature calibration procedure was performed by using the same set-point temperature for the pre-cooling of the inlet and the cold plate. Hereby, 13 images were recorded at uniform temperatures ranging from 17 to 5 °C. Unfortunately, it was not possible to reach a bulk temperature below 5 °C in our experimental setup. Therefore, the obtained fit for the temperature calibration was extrapolated in order to include the temperatures in the range from 0 to 5 °C.

Table 2
Temperature calibration data.

Average intensity ratio	Relative standard deviation	Temperature
1.0222%	3.29%	17.0 ± 0.2 °C
1.0405%	4.53%	16.0 ± 0.2 °C
1.07416%	10.55%	15.0 ± 0.2 °C
1.09484%	6.08%	14.0 ± 0.2 °C
1.10848%	6.06%	13.1 ± 0.2 °C
1.13094%	6.48%	12.1 ± 0.2 °C
1.14077%	7.22%	11.2 ± 0.2 °C
1.17054%	7.35%	10.1 ± 0.2 °C
1.19784%	7.51%	8.9 ± 0.2 °C
1.21764%	7.69%	7.9 ± 0.2 °C
1.124342%	7.92%	7.0 ± 0.2 °C
1.26958%	7.97%	6.0 ± 0.2 °C
1.28080%	7.87%	5.3 ± 0.2 °C

The images were pre-processed using the procedure outlined in Section 2.6, and the average intensity ratio in the area of interest was calculated. The temperature calibration data points are given in Table 2 and plotted in Fig. 5. The standard deviation in the average intensity ratio was attributed to the noise present in our measurements (and therefore not considered to be a result of spatio/temporal temperature variation within the area of interest during a single temperature calibration measurement). The temperature intensity-ratio relationship is described by the following linear relationship:

$$T\ [°C] = a(I_R - 1.0) + b \tag{8}$$

The coefficients of the fit were found using the orthogonal distance regression algorithm [36], which is capable of taking into account both the uncertainties in the intensity ratio data and the uncertainties in the temperature (since the thermo-couples have an uncertainty of 0.2 °C): $a = -45.9 \pm 0.8$ K, $b = 18.1 \pm 0.1$ K.

The experimental campaign was performed over the course of roughly two months, during which the same calibration was used. To correct for possible changes to the experimental conditions (such as quenching of the dye, a change in the concentration ratio or the presence of a reflective ice layer), a constant correction factor was used. At the start of the experiment, the temperature above the half-width of the channel should be equal to the bulk temperature (from now on referred to as the region of reference). For the center of the channel (between $x = 70$ cm and $x = 80$ cm), we defined the region of reference (ROR) to be $[x_0 : x_{end}, y_0 : y_{end}] = [-20 : 20, 25 : 45]$ mm^2. The expected bulk temperature T_0 can be obtained from the inlet and outlet temperatures (as measured by the thermo-couples). Using the

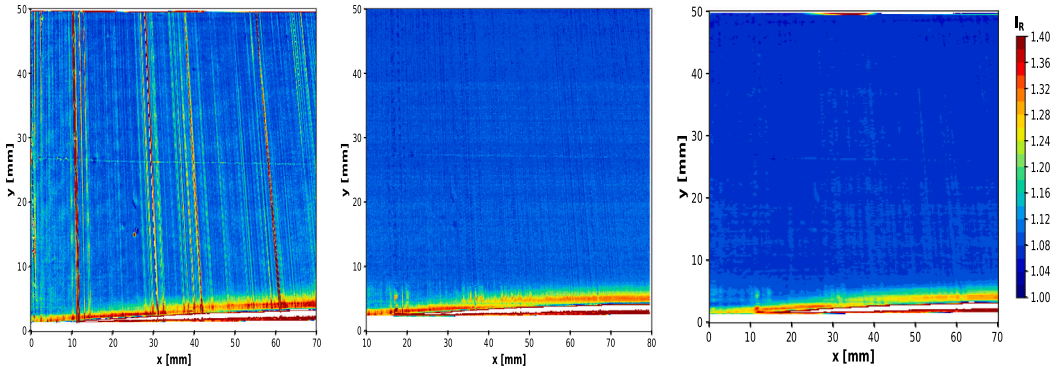

(a) Intensity ratio map after pre-processing.

(b) Intensity ratio map after striation removal through LOF algorithm.

(c) Intensity ratio map after smoothing.

Fig. 4. Intensity ratio map after the different postprocessing steps (pre-processing (a), striation removal (b), smoothing (c)), taken at the inlet of the test-section for $t = 5$ min after the onset of ice-formation. The experimental settings were: $Re \approx 474$, $T_{in,set} = 15$ °C and $T_{c,set} = -10$ °C.

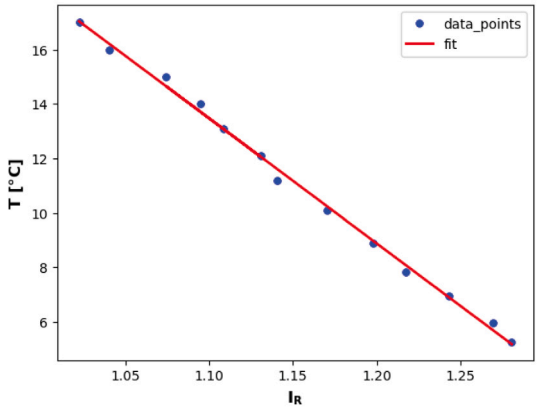

Fig. 5. Temperature calibration curve.

calibration, the bulk temperature is converted to an intensity ratio $I_{R,0}$ using Eq. (8):

$$T_0\ [^\circ\mathrm{C}] = a\left(I_{R,0} - 1.0\right) + b \tag{9}$$

$$\frac{T_0}{a} + 1.0 - \frac{b}{a} = I_{R,0}. \tag{10}$$

The expected intensity ratio is compared with the average intensity ratio in the region of reference from the LIF measurements ($\overline{I}_{R,ROR}$). Subsequently, the correction factor is calculated as

$$C_F = \frac{I_{R,0}}{\overline{I}_{R,ROR}} \tag{11}$$

and the intensity ratio is corrected as:

$$\tilde{I}_R = C_F \times I_R. \tag{12}$$

The corrected temperatures are thus calculated as:

$$T\ [^\circ\mathrm{C}] = a(\tilde{I}_R - 1.0) + b = a\left(\frac{I_{R,0}}{\overline{I}_{R,ROR}} I_R - 1.0\right) + b. \tag{13}$$

2.8. Uncertainty quantification

Using the formula for the propagation of uncertainties, the uncertainty in the temperature is derived from Eq. (13):

$$\sigma_T^2\ [^\circ\mathrm{C}] = \left(\frac{\partial T}{\partial a}\right)^2 \sigma_a^2 + \left(\frac{\partial T}{\partial b}\right)^2 \sigma_b^2 + \left(\frac{\partial T}{\partial \tilde{I}_R}\right)^2 \sigma_{\tilde{I}_R}^2$$

$$= \underbrace{\left[(\tilde{I}_R - 1.0)\sigma_a\right]^2 + \sigma_b^2}_{\sigma_{T,cal}} + \underbrace{(a\sigma_{\tilde{I}_R})^2}_{\sigma_{T,\tilde{I}_R}}. \tag{14}$$

The total uncertainty can be split into an uncertainty in the temperature calibration and an uncertainty in the measured (corrected) intensity ratio. The uncertainty in the temperature calibration is obtained from the uncertainties in the fit coefficients ($\sigma_a \approx 0.8$ °C and $\sigma_b \approx 0.1$ °C) and translates into a temperature uncertainty of approximately $\sigma_{T,cal} = 0.15$ °C for a temperature of $T = 15$ °C.

The uncertainty in the corrected intensity ratio $\sigma_{\tilde{I}_R}$, is derived from Eq. (12):

$$\sigma_{\tilde{I}_R}^2 = \left(\frac{\partial \tilde{I}_R}{\partial C_F}\right)^2 \sigma_{C_F}^2 + \left(\frac{\partial \tilde{I}_R}{\partial I_R}\right)^2 \sigma_{I_R}^2 = (I_R\sigma_{C_F})^2 + (C_F\sigma_{I_R})^2. \tag{15}$$

As such, the uncertainty in the corrected intensity ratio is determined by both the uncertainty in the correction factor and the uncertainty in the measured (uncorrected) intensity ratio. The uncertainty in the measured (uncorrected) intensity ratio σ_{I_R} consists of a statistical and a systematic uncertainty contribution:

$$\sigma_{I_R}^2 = \sigma_{I_{R,stat}}^2 + \sigma_{I_{R,sys}}^2 \tag{16}$$

The statistical uncertainty originates from factors such as the camera noise or fluctuations in the laser intensity. The statistical contribution to σ_{I_R} is calculated as

$$\sigma_{I_{R,stat}}^2 = \frac{1}{N_t N_x N_y (N_t - 1)} \sum_{i=1}^{N_t} \left(I_{R_i} - \overline{I}_R\right)^2, \tag{17}$$

where $N_t = 25$ is the number of samples used for the time-averaging, and N_x, N_y are the number of pixels in the x- and y-direction over which the smoothing operation is performed.[2]

The systematic uncertainty originates from the presence of artefacts such as the striations and the sensitivity of the camera. The systematic uncertainty is estimated by calculating the standard deviation within the region of reference (ROR) where a uniform intensity ratio is expected, and subtracting the statistical uncertainty:

$$\sigma_{I_{R,sys}}^2 = \left(\frac{1}{N_{ROR}(N_{ROR} - 1)} \sum_{i=1}^{N_{ROR}} \left(I_{R_i} - \overline{I}_{R,ROR}\right)^2\right) - \sigma_{I_{R,stat}}^2, \tag{18}$$

[2] Using a larger averaging window in either time or space will reduce the statistical error (and also require either more time samples or result in the loss of spatial resolution), since we consider the statistical uncertainty to be caused by random fluctuations in quantities such as the camera pixel gain or the laser intensity which cancel each other out upon averaging.

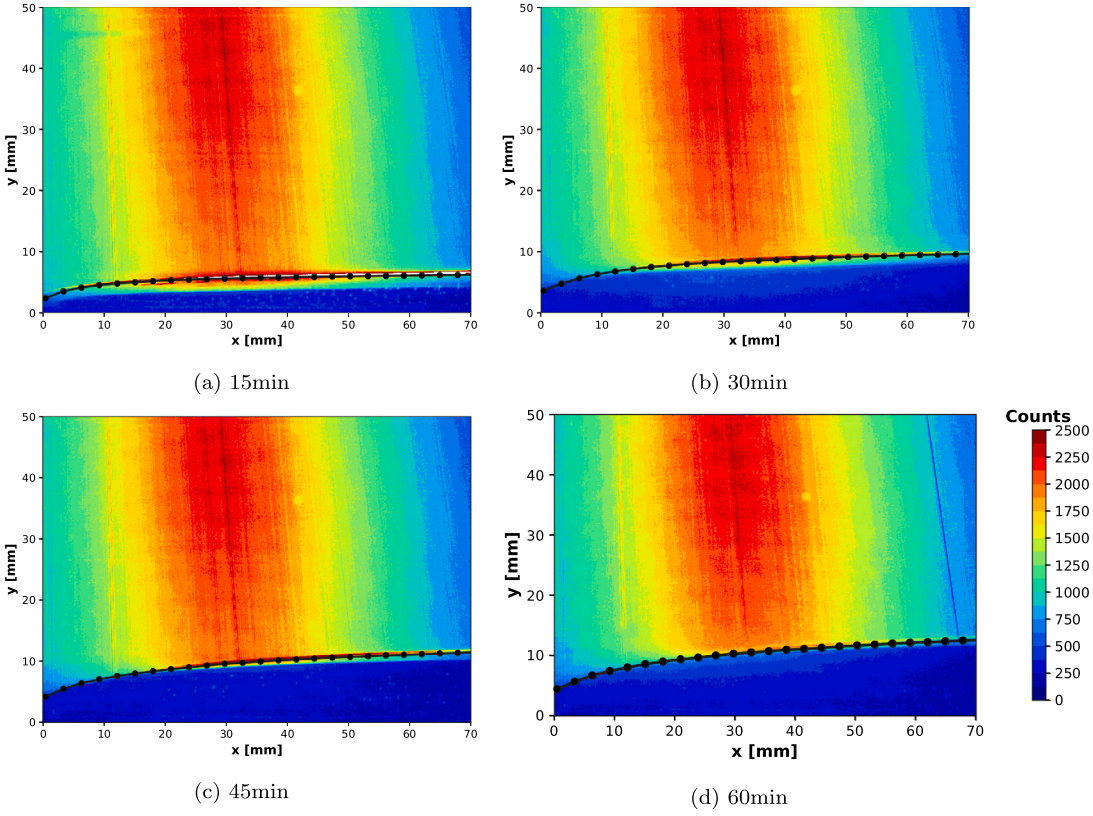

Fig. 6. Intensity counts for camera α (detecting the emission intensity of Rhodamine B) after respectively 15, 30, 45 and 60 min of ice-growth. The experimental settings were: $Re \approx 474$, $T_{in,set} = 0.5$ °C and $T_{c,set} = -10$ °C. The ice growth measurements from the previous PIV campaign are plotted in white [13].

where N_{ROR} is the number of data points in the ROR. We consider the estimated systematic uncertainty within the region of reference to be representative of the systematic error within the entire area of interest.

Finally, the uncertainty in the correction factor is derived from Eq. (11):

$$\sigma_{C_F}^2 = \left(\frac{\partial C_F}{\partial I_{R,0}}\right)^2 \sigma_{I_{R,0}}^2 + \left(\frac{\partial C_F}{\partial \overline{I}_{R,ROR}}\right)^2 \sigma_{\overline{I}_{R,ROR}}^2 = \left(\frac{1}{\overline{I}_{R,ROR}}\sigma_{I_{R,0}}\right)^2 + \left[\left(\frac{I_{R,0}}{\overline{I}_{R,ROR}^2}\right)\sigma_{\overline{I}_{R,ROR}}\right]^2. \quad (19)$$

The uncertainty in the average intensity in the window of reference $\overline{I}_{R,ROR}$ is calculated as

$$\sigma_{\overline{I}_{R,ROR}}^2 = \frac{\frac{1}{N_{ROR}(N_{ROR}-1)}\sum_{i=1}^{N_{ROR}}\left(I_{R_i} - \overline{I}_{R,ROR}\right)^2}{N_{ROR}}. \quad (20)$$

The uncertainty the reference intensity $I_{R,0}$ is calculated as

$$\sigma_{I_{R,0}}^2 = \left(\frac{\partial I_{R,0}}{\partial T_0}\right)^2 \sigma_{T_0}^2 + \left(\frac{\partial I_{R,0}}{\partial a}\right)^2 \sigma_a^2 + \left(\frac{\partial I_{R,0}}{\partial b}\right)^2 \sigma_b^2 = \left(\frac{1}{a}\sigma_{T_0}\right)^2 + \left(\frac{T_0 - b}{a^2}\sigma_a\right)^2 + \left(\frac{1}{a}\sigma_b\right)^2, \quad (21)$$

where $\sigma_{T_0} = 0.2$ °C (the uncertainty in the thermo-couple). The contribution from the uncertainty in the measured (corrected) intensity ratio amounts to approximately $\sigma_{T,\tilde{I}_R} \approx 0.3$ °C, but may vary across the different measurements.

Another possible source of uncertainty was the thermal effect of the laser, which was estimated through:

$$\Delta T = \frac{Q_{laser} \times t_{pulse}}{\rho c_p \phi_v \times t_{sample}} = 0.067 \text{ K}. \quad (22)$$

This value (which is well below the calculated uncertainties in the temperature calibration and the temperature measurements) is a significant overestimation, since it assumes that all the laser energy is converted into heat and does not account for the laser energy which is lost to the environment. Therefore, the thermal effect of the laser is considered to be negligible in this study.

3. Results and discussion

3.1. Observing the transient growth of an ice-layer using laser induced fluorescence

Fig. 6 shows the image intensities for camera α (corresponding to the temperature sensitive dye Rhodamine B), after respectively 15, 30, 45 and 60 min of ice-growth. The experimental settings were: $Re \approx 474$, $T_{in,set} = 0.5$ °C and $T_{c,set} = -10$ °C. The highest intensities were observed between $x = 20$ mm and $x = 40$ mm, where the laser sheet is centered. Several top to bottom striations were present in the raw LIF images from camera α. These striations were not eliminated upon calculating the intensity ratio between the images of camera α and camera β, and therefore need to be removed using the proposed post-processing procedure described in Section 2.6.

The ice has a significantly lower fluorescence emission intensity compared to the liquid water above. We believe this is both because of the scattering of the laser light by the ice–water interface and due to the fact that the concentration of Rhodamine B (and also Rhodamine 110) is significantly lower in the ice than in the water as a result of the rejection of the dyes during the crystallization process, leaving the dyes behind in the solution. This hypothesis is supported by the transparent color of the ice in our experiments, whilst the liquid water had a red-greenish color from the dissolved dyes. Based on this observation, we therefore recommend using two color LIF for solid–liquid phase change

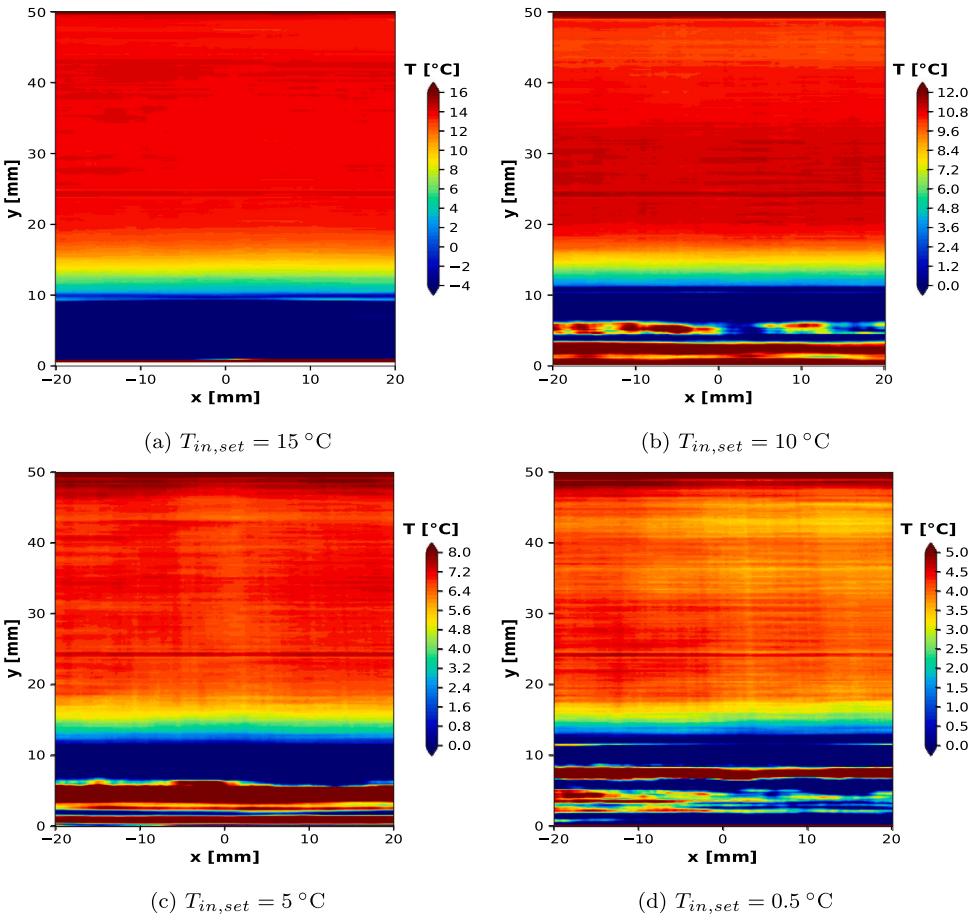

Fig. 7. LIF temperature field measurements at the center of the channel after 30 min of ice growth, for different inlet temperature conditions.

experiments, especially for freezing or melting in an enclosure where the phase change may significantly affect the dye concentrations.[3]

For comparison purposes, the ice-layer thickness measurements from our previous PIV campaign [13] was plotted on top of the LIF image intensities. A good match was observed between the scattering signal of the laser light from the ice–water interface (characterized by a high intensity line following the curvature of the ice layer) and the PIV ice layer measurements. Therefore, in principle it is possible to use the scattering of the laser by the ice–water interface to determine its position. However, very close to the inlet (within roughly the first 10 to 25 mm depending on the time after the onset of ice-formation) no clear LIF signal from the scattering of the laser could be observed. Alternatively, the location of the ice-layer can be determined based on $T = 0$°C. However, the scattering of the laser light may pose a challenge for an accurate measurement of the temperature within in the thermal boundary layer, as shown in Section 3.2 and by Gong et al. and [17] who described similar challenges. Therefore, whenever possible we recommend using an alternative technique for determining the solid–liquid interface (such as PIV), due to the associated difficulties with using LIF for interface tracking. Please also refer to Voulgorapoulos et al. [12] who conducted early-stage experimental trials attempting to use LIF for locating the solid–liquid interface and concluded that a more accurate and reliable tracking methodology could be established when using PIV.

[3] We would like to point out that Gong et al. used one-color LIF for measuring the temperature fields during the melting of n-octadecane in a cuboid enclosure, possibly influencing the results especially towards the end of the experiment.

3.2. LIF temperature measurements

Fig. 7 shows the LIF temperature measurements at the center of the channel for four different set points of the inlet temperature, these are $T_{in,set}$ = 15 °C, $T_{in,set}$ = 10 °C, $T_{in,set}$ = 5 °C and $T_{in,set}$ = 0.5 °C. The in and outlet temperatures measured by the thermo-couples, as well as the used correction factors, are given in Table 3. Overall, qualitatively promising results were obtained. The thermal boundary layer is clearly visible above the ice, demonstrating the potential of LIF as a non-intrusive temperature measurement techniques. Even for the smallest set point temperature of $T_{in,set}$ = 0.5 °C (where the actual inlet temperature is approximately equal to 4.7 °C and the outlet temperature is around 4.5 °C resulting in a temperature difference of around 4.5–4.7 °C between the bulk and the melting point), the thermal boundary layer can be distinguished, indicating an adequate temperature resolution of the technique. Consistent with expectations, the temperature variation in the x-direction is very small. Despite the promising results, we would like to note that the post-processing involved the removal of 50% to 30% of the data points (which were considered to be outliers) for the center and inlet of the channel respectively, as well as a significant amount of smoothing (as shown in Section 2.6), in particular for the x-direction. As such, the applied post-processing procedure, whilst successfully reducing the noise level, also resulted in significant loss of information and loss of spatial resolution.

For the smallest temperature range, the relative uncertainty was quite significant at about 10%. In addition, the absolute temperature uncertainty was higher for the smaller temperature ranges (around σ = 0.5 °C for $T_{in,set}$ = 0.5 °C compared to σ = 0.3 °C for $T_{in,set}$ = 15 °C). This is caused by a smaller signal to noise ratio, resulting in a less efficient removal of the top to bottom striations using the local outlier

Table 3
Correction factor and representative uncertainty.

Location	$T_{in,set}$	ϕ_v (L s^{-1})	T_{in} (°C)	T_{out} (°C)	Correction factor	$\overline{\sigma}_T$
Center	15 °C	0.038 ± 0.004	14.60 ± 0.04	13.7 ± 0.4	1.009 ± 0.005	0.3 °C
	10 °C	0.038 ± 0.004	10.73 ± 0.04	10.1 ± 0.2	1.023 ± 0.005	0.4–0.5 °C
	5 °C	0.037 ± 0.004	6.9 ± 0.2	6.8 ± 0.3	1.030 ± 0.005	0.4–0.6 °C
	0.5 °C	0.036 ± 0.007	4.7 ± 0.2	4.6 ± 0.3	1.020 ± 0.006	0.5 °C
Inlet	15 °C	0.038 ± 0.004	14.56 ± 0.05	13.6 ± 0.4	1.008 ± 0.005	0.3–0.4 °C
	10 °C	0.037 ± 0.004	10.56 ± 0.02	10.26 ± 0.07	0.999 ± 0.005	0.5 °C
	5 °C	0.036 ± 0.004	6.7 ± 0.1	6.4 ± 0.2	0.999 ± 0.005	0.5 °C
	0.5 °C	0.036 ± 0.004	4.71 ± 0.07	4.5 ± 0.3	1.015 ± 0.005	0.6 °C

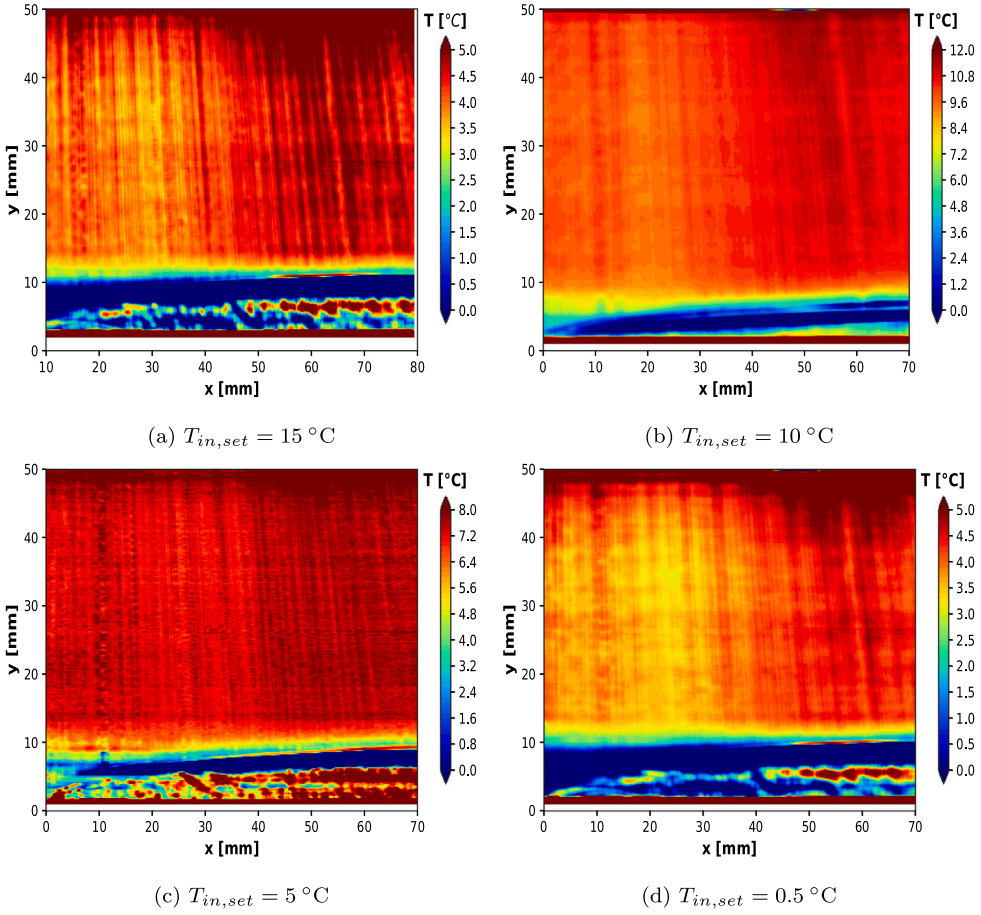

Fig. 8. LIF temperature field measurements at the inlet of the channel after 30 min of ice growth, for different inlet temperature conditions.

factor algorithm, as well as a higher uncertainty in the temperature calibration at the lowest temperatures (recall that the uncertainty in the calibration scales with the intensity ratio, which is higher at lower temperatures, as shown in Section 2.8).

Fig. 8 shows the temperature measurements at the inlet of the channel. Compared to the measurements at the center, the measurements at the inlet were more challenging because the curvature of the ice-layer introduced additional noise due to the scattering of the laser light, and because the variation of the temperature in the x-direction resulted in a more troublesome removal of the striations (and other outliers), with a smaller degree of smoothing being applied (as shown in Section 2.6). In addition, the thermal boundary layer above the ice-layer is thinner. Although the thermal boundary layer above the ice-layer is visible for all four measurements, the results are relatively noisy. For Figs. 8(a) and (b), a temperature artefact was observed near the top of the channel at $y = 50$ mm. This was attributed to reflections of the laser light from the top lid, resulting in noisy measurements near the top of the channel. In addition, artefacts were present within the thermal boundary layer, as a result of the scattering of the laser light by the ice-layer. Compared to the center of the channel, the scattering of the laser light by the ice-layer induced a higher level of noise for the measurements at the inlet of the channel, since the ice-layer was curved instead of (almost) flat (also see Fig. 6). These artefacts were not removed by the postprocessing algorithm and subsequently led to unphysical oscillations of the LIF temperature measurements within the thermal boundary layer.

Fig. 9 shows the temperature profiles for two different inlet temperatures, i.e. $T_{in} = 15$ °C and $T_{in} = 0.5$ °C, for both the inlet and the center of the channel. For $T_{in} = 15$ °C, good results were obtained. Especially for the center of the channel at $x = 75$ cm, the relative temperature uncertainty appears to fall within an acceptable range, with smooth temperature profiles obtained and a sufficiently high temperature resolution within the thermal boundary layer. However, for the inlet of the channel, some of the data points within the thermal boundary layer were removed, as a result of unphysical oscillations within the LIF temperature measurements, attributed to a high level of noise induced by the scattering of the laser light by the ice–water interface. This unphysical behavior was not included in our uncertainty

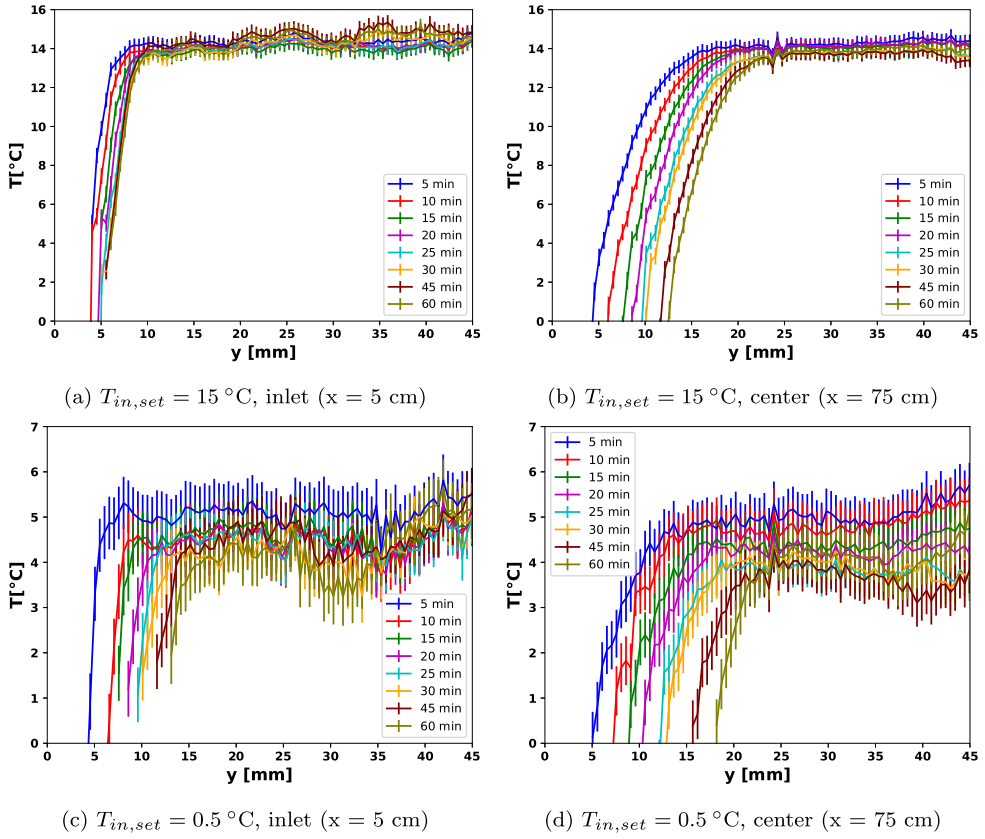

(a) $T_{in,set} = 15\,^{\circ}\mathrm{C}$, inlet (x = 5 cm) (b) $T_{in,set} = 15\,^{\circ}\mathrm{C}$, center (x = 75 cm)

(c) $T_{in,set} = 0.5\,^{\circ}\mathrm{C}$, inlet (x = 5 cm) (d) $T_{in,set} = 0.5\,^{\circ}\mathrm{C}$, center (x = 75 cm)

Fig. 9. LIF temperature profiles at the inlet and the center of the channel for two different inlet temperatures, i.e. $T_{in,set} = 15\,^{\circ}\mathrm{C}$ and $T_{in,set} = 0.5\,^{\circ}\mathrm{C}$ Results are shown for both the inlet and the center of the channel. For the inlet of the channel, the data points corresponding to unphysical oscillations of the LIF temperature measurements within the thermal boundary layer have been removed.

analysis. Compared to the center of the channel, a steeper temperature gradient is observed within the temperature boundary layer near the inlet, which is consistent with the expected thinner thermal boundary layer for the thermal entrance region of the channel.

In addition, for the smallest temperature range with $T_{in} = 0.5\,^{\circ}\mathrm{C}$, the relative uncertainty is approximately ±10%, resulting in less smooth temperature profiles. For such small temperature ranges, improvements to the present setup are needed in order to reduce the signal to noise ratio and perform sufficiently accurate LIF temperature measurement results which can be used for numerical benchmarking purposes. These improvements should consist of less air-bubbles and a lid specially designed to ensure optimal transition of the laser, an improved optical setup (for instance by using a double-pulsed laser, using cameras with a larger dynamic range or by changing the dyes or filters to achieve a better separation between the spectra in each camera image) or an additional post-processing routine to reduce the noise caused by the scattering of the laser light from the ice–water interface. A further increase in the accuracy of the two-color LIF temperature measurements could be obtained through optimization of the concentration (ratio) of the dyes and/or the optical parameters used (such as the duration of the laser pulse and the aperture), or through reducing the uncertainty of the temperature calibration procedure by increasing the number of calibration data points.

3.3. Temperature measurement in the lag time prior to freezing

Consistent with our previous PIV campaign [13] and the results obtained by Savino et al. [32], the onset of freezing was marked by a rapid spreading of ice over the entire cold plate, accompanied by a sudden increase of the cold plate temperature, as can be seen in Fig. 10. Thermocouple 0 at the inlet of the channel is the first to experience a sudden temperature increase, and the ice nucleus is shown to propagate at a near constant velocity of approximately 5 $\mathrm{cm\,s^{-1}}$ towards the exit of the channel, as shown by the quasi linear relationship between the different time-instances at which the thermocouples notice the effect of phase change. The total delay between the response of thermocouple 7 at the end of the cold plate and thermocouple 0 at the inlet was less than 30 s. Freezing only occurred after the cold plate had reached a subzero temperature of between −4 and −6 °C for an inlet temperature of $T = 15\,^{\circ}\mathrm{C}$. Previously, Savino et al. had presented evidence of subcooling within the thermal boundary layer of the liquid [32], collected through a thermocouple probe before the formation of ice occurred.

The present experimental campaign is the first to present non-intrusive temperature measurements within the thermal boundary layer prior to the start of the freezing process. Fig. 11 shows the temperature profiles at the center of the test section in the moments before the onset of ice-formation, for $T_{in,set} = 15\,^{\circ}\mathrm{C}$. Consistent with the experiments of Savino et al., a subcooling of approximately 2 °C was observed. We therefore recommend including the presence of subcooling before the spreading of ice over the cold plate in numerical models of freezing in internal flow.

In addition, a very interesting behavior was observed within the thermal boundary layer prior to ice formation (for $t \approx -2.5$ min and $t \approx -10$ s). These temperature profiles clearly depart from the expected behavior for the thermal boundary layer in (almost) fully developed channel flow, with a smaller temperature gradient than expected in the first few mm above the cold plate and a point of inflection at approximately $y = 5$ mm. This point of inflection was not present for longer times prior to ice formation (i.e. $t \approx -4.5$ min) and for the measurements taken during the growth of the ice-layer (see Fig. 9). This point of inflection appears to build up in the time-span leading up to the sudden formation of ice, at which ice rapidly spreads over the entire cold plate.

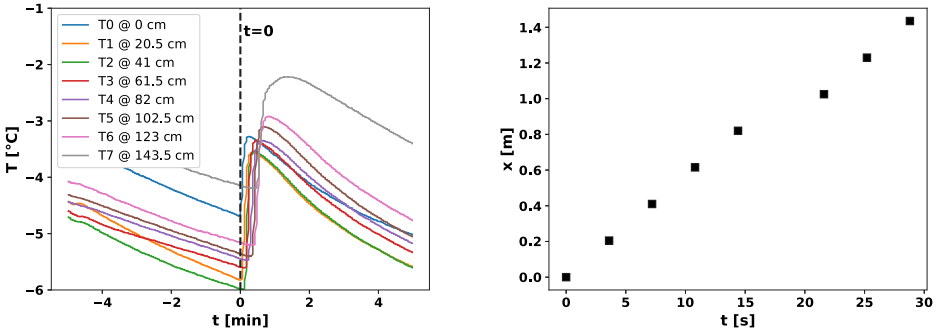

Fig. 10. Cold plate temperature response in the 5 min before and after the onset of freezing (a), for $T_{in,set}$ = 15 °C. T0–T7 refer to the different locations of the thermocouples. Propagation of the ice nucleus from the inlet to the exit of the channel (b). The vertical axis denotes the location of the thermocouples and the horizontal axis denotes the time after which the first thermocouple (T0) recorded the onset of freezing.

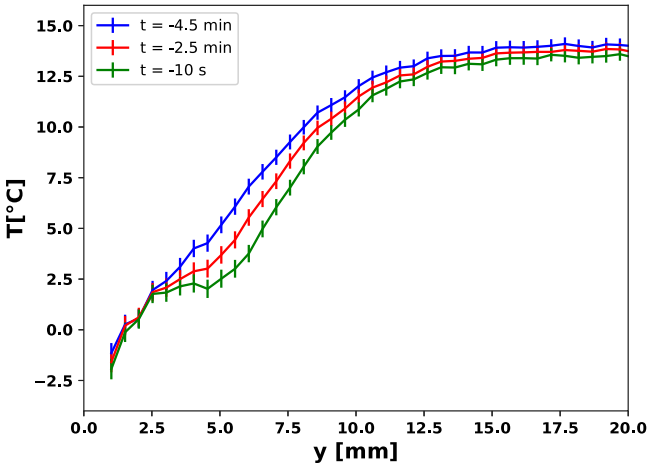

Fig. 11. LIF temperature profiles for $T_{in,set}$ = 15 °C at the center of the channel (x = 75 cm), taken for various times prior to the onset of ice formation.

The anomalous temperature behavior is possibly related to an enhanced natural convection, occurring as a result of the subcooling of the water at the cold plate surface, as was previously suggested by Mulligan et al. [37]. Mulligan et al. performed an experimental study of the steady-state ice deposition in a laminar pipe flow with a cooled tube wall, and observed a decrease in the heat transfer rate at the wall as its temperature dropped below the freezing point. Similarly, we observed a faster decrease in the cold-plate temperature after the onset of ice formation compared to before (see Fig. 10).

For future work we recommend additional non-intrusive temperature measurements as part of a more detailed investigation of the anomalous temperature behavior prior to the onset of freezing. Performing these measurements at appropriate time intervals is challenging, since the exact moment at which freezing occurs is not known a-priori. Moreover, by performing combined temperature and velocity measurements in the moments prior to the onset of ice-formation (for instance through a combination of PIV and LIF, see Funatani et al. [21]), confirmation can be obtained as to whether the anomalous temperature behavior is indeed caused by enhanced natural convection as a result of subcooling at the cold plate surface.

4. Conclusions

This work presents two color LIF temperature measurements for the transient freezing in a square channel for laminar flow conditions ($Re \approx 474$), for four different set-points of the inlet temperature ($T_{in,set}$ = 15°C, $T_{in,set}$ = 10 °C, $T_{in,set}$ = 5 °C and $T_{in,set}$ = 0.5 °C). LIF has only been used once before for solid–liquid phase change experiments by Gong et al. [17], for measuring the temperature distribution of melting n-octadecane in a cuboid cavity. Important novelties of the present LIF campaign were the use of a two color (instead of a one color) LIF technique to compensate for a possible change in dye concentration and optics during ice growth, the use of a post-processing algorithm to remove striations and other artefacts, and a detailed analysis of the uncertainty in the measured temperature fields. In addition, this work presents the first measurements of the temperature distributions within the thermal boundary layer both during and prior to the transient freezing of a liquid in a laminar channel flow.

Measurements were performed at both the inlet and the center of the test section. The postprocessing involved the use of the local outlier factor algorithm followed by a smoothing operation using a moving average window. In addition, a correction factor was used to reduce the temperature bias as a result of variations in experimental conditions throughout the experimental campaign. Our approach resulted in an absolute temperature uncertainty of between σ = 0.3 °C and σ = 0.5 °C which is comparable to related LIF temperature measurement campaigns.

The primary aim of this work was to demonstrate the potential and limitations of LIF as a non-intrusive temperature measurement technique for solid liquid phase change experiments. We showed that good results could be obtained for a sufficiently large temperature range of approximately 15 °C in our case. For a small temperature ranges of approximately 5 °C however, the large relative uncertainty in the temperature deteriorated the quality of the results. In addition, the scattering of the laser light from the ice layer introduced some artefacts, especially near the inlet of the channel where the ice–water interface is curved instead of flat. As such, further improvements are needed to use LIF to generate high fidelity experimental data for numerical validation purposes. Some suggested improvements are to ensure a very clean entry surface for the laser sheet (without air bubbles, dirt particles or surface roughness), to use a camera with a large dynamic range and to improve the post-processing such that the noise as a result of the scattering of the laser light by the ice-layer can be removed.

LIF temperature measurements within the thermal boundary layer taken within a short time span prior to the onset of ice formation showed approximately 2 °C of subcooling, consistent with the findings of Savino et al. [32]. The onset of ice formation was accompanied by a sudden increase in the cold plate temperature (used to determine t = 0 in our experiments). The thermocouple recordings of the cold plate showed that the ice nucleus propagated from the inlet to the exit of the channel at a near constant velocity of approximately 5 cm s^{-1} for the given flow conditions (Re = 474, $T_{in,set}$ = 15 °C, $T_{c,set}$ = −10 °C). Based on these findings, we recommend that subcooling effects are taken into account in numerical models of ice growth in internal flow.

In addition, an anomalous behavior within the thermal boundary layer was observed, with a significantly smaller temperature gradient within the first few mm above the cold plate than would be expected for fully developed channel flow, and a point of inflection around $y = 5$ mm. Possibly, the anomalous temperature behavior was caused by an enhanced natural convection as a result of the subcooling within the thermal boundary layer. This hypothesis could be confirmed by PIV measurements taken within a short time span before ice growth starts to occur.

CRediT authorship contribution statement

Bouke Johannes Kaaks: Conceptualization, Formal analysis, Investigation, Methodology, Validation, Writing – original draft, Writing – review & editing. **Sebastian Couweleers:** Methodology. **Danny Lathouwers:** Funding acquisition, Supervision, Writing – review & editing. **Jan-Leen Kloosterman:** Funding acquisition, Supervision, Writing – review & editing. **Martin Rohde:** Conceptualization, Funding acquisition, Resources, Supervision, Validation, Writing – review & editing.

Declaration of competing interest

The authors declare the following financial interests/personal relationships which may be considered as potential competing interests: B.J. Kaaks reports financial support was provided by Euratom Research and Training Programme. If there are other authors, they declare that they have no known competing financial interests or personal relationships that could have appeared to influence the work reported in this paper.

Data availability

The raw data from the LIF measurements can be found under the associated link:

Experimental dataset referring to: Non-intrusive temperature measu rements for transient freezing in laminar internal flow using laser i nduced fluorescence (Original data) (Zenodo).

Acknowledgments

This project has received funding from the Euratom research and training programme 2014–2018 under grant agreement no. 847527.

References

[1] C. Gau, R. Viskanta, Melting and solidification of a Pure Metal on a Vertical Wall, J. Heat Transfer 108 (1986) 174–181.

[2] T.A. Campbell, J.N. Koster, Visualization of liquid-solid interface morphologies in gallium subject to natural convection, J. Cryst. Growth (ISSN: 00220248) 140 (3–4) (1994) 414–425, http://dx.doi.org/10.1016/0022-0248(94)90318-2.

[3] O. Ben-David, A. Levy, B. Mikhailovich, A. Azulay, 3D numerical and experimental study of gallium melting in a rectangular container, Int. J. Heat Mass Transfer (ISSN: 0017-9310) 67 (2013) 260–271, http://dx.doi.org/10.1016/j.ijheatmasstransfer.2013.07.058.

[4] J. Vogel, D. Bauer, Phase state and velocity measurements with high temporal and spatial resolution during melting of n -octadecane in a rectangular enclosure with two heated vertical sides, Int. J. Heat Mass Transfer (ISSN: 0017-9310) 127 (2018) 1264–1276, http://dx.doi.org/10.1016/j.ijheatmasstransfer.2018.06.084.

[5] M. Faden, C. Linhardt, S. Höhlein, A. König-Haagen, D. Brüggemann, Velocity field and phase boundary measurements during melting of n-octadecane in a cubical test cell, Int. J. Heat Mass Transfer (ISSN: 00179310) 135 (2019) 104–114, http://dx.doi.org/10.1016/j.ijheatmasstransfer.2019.01.056.

[6] G. Cartland Glover, A. Skillen, D. Litskevich, S. Rolfo, D.R. Emerson, B. Merk, C. Moulinec, On the numerical modelling of frozen walls in a molten salt fast reactor, Nucl. Eng. Des. (ISSN: 00295493) 355 (March) (2019) 110290, http://dx.doi.org/10.1016/j.nucengdes.2019.110290.

[7] M. Tiberga, D. Shafer, D. Lathouwers, M. Rohde, J.L. Kloosterman, Preliminary investigation on the melting behavior of a freeze-valve for the Molten Salt Fast Reactor, Ann. Nucl. Energy (ISSN: 18732100) 132 (2019) 544–554, http://dx.doi.org/10.1016/j.anucene.2019.06.039.

[8] B.J. Jones, D. Sun, S. Krishnan, S.V. Garimella, Experimental and numerical study of melting in a cylinder, Int. J. Heat Mass Transfer (ISSN: 00179310) 49 (15–16) (2006) 2724–2738, http://dx.doi.org/10.1016/j.ijheatmasstransfer.2006.01.006.

[9] Z. Lipnicki, B. Weigand, An experimental and theoretical study of solidification in a free-convection flow inside a vertical annular enclosure, Int. J. Heat Mass Transfer (ISSN: 00179310) 55 (4) (2012) 655–664, http://dx.doi.org/10.1016/j.ijheatmasstransfer.2011.10.044.

[10] M.Z.M. Rizan, F.L. Tan, C.P. Tso, An experimental study of n-octadecane melting inside a sphere subjected to constant heat rate at surface, Int. Commun. Heat Mass Transfer (ISSN: 07351933) 39 (10) (2012) 1624–1630, http://dx.doi.org/10.1016/j.icheatmasstransfer.2012.08.003.

[11] T.A. Kowalewski, M. Rebow, Freezing of water in a differentially heated cubic cavity, Int. J. Comput. Fluid Dyn. (ISSN: 10618562) 11 (3–4) (1999) 193–210, http://dx.doi.org/10.1080/10618569908940874.

[12] V. Voulgaropoulos, N.L. Brun, A. Charogiannis, C.N. Markides, Transient freezing of water between two parallel plates: A combined experimental and modelling study, Int. J. Heat Mass Transfer (ISSN: 00179310) 153 (2020) 119596, http://dx.doi.org/10.1016/j.ijheatmasstransfer.2020.119596.

[13] B.J. Kaaks, D. Lathouwers, J.-L. Kloosterman, M. Rohde, Transient freezing of water in a square duct: Anexperimental benchmark, SSRN Electron. J. (2023) http://dx.doi.org/10.2139/ssrn.4360285.

[14] F.L. Tan, Constrained and unconstrained melting inside a sphere, Int. Commun. Heat Mass Transfer 35 (4) (2008) 466–475.

[15] Z. Chen, D. Gao, J. Shi, Experimental and numerical study on melting of phase change materials in metal foams at pore scale, Int. J. Heat Mass Transfer (ISSN: 00179310) 72 (2014) 646–655, http://dx.doi.org/10.1016/j.ijheatmasstransfer.2014.01.003.

[16] V. Kumar, M. Kumawat, A. Srivastava, S. Karagadde, Mechanism of flow reversal during solidification of an anomalous liquid, Phys. Fluids (ISSN: 10897666) 29 (12) (2017) http://dx.doi.org/10.1063/1.5005139.

[17] W. Gong, Heat storage of PCM inside a transparent building brick : Experimental study and LBM simulation on GPU Heat storage of PCM inside a transparent building brick : experimental study and LBM simulation on GPU (Ph.D. thesis), INSA de Lyon, 2015.

[18] J. Sakakibara, R.J. Adrian, Whole field measurement of temperature in water using two-color laser induced fluorescence, Exp. Fluids (ISSN: 07234864) 26 (1–2) (1999) 7–15, http://dx.doi.org/10.1007/s003480050260.

[19] F. Lemoine, Y. Antoine, M. Wolff, M. Lebouche, Simultaneous temperature and 2D velocity measurements in a turbulent heated jet using combined laser-induced fluorescence and LDA, Exp. Fluids (ISSN: 07234864) 26 (4) (1999) 315–323, http://dx.doi.org/10.1007/s003480050294.

[20] M. Bruchhausen, F. Guillard, F. Lemoine, Instantaneous measurement of two-dimensional temperature distributions by means of two-color planar laser induced fluorescence (PLIF), Exp. Fluids (ISSN: 07234864) 38 (1) (2005) 123–131, http://dx.doi.org/10.1007/s00348-004-0911-2.

[21] S. Funatani, N. Fujisawa, H. Ikeda, Simultaneous measurement of temperature and velocity using two-colour LIF combined with PIV with a colour CCD camera and its application to the turbulent buoyant plume, Meas. Sci. Technol. (ISSN: 09570233) 15 (5) (2004) 983–990, http://dx.doi.org/10.1088/0957-0233/15/5/030.

[22] S. Grafsronningen, A. Jensen, Simultaneous PIV/LIF measurements of a transitional buoyant plume above a horizontal cylinder, Int. J. Heat Mass Transfer (ISSN: 00179310) 55 (15–16) (2012) 4195–4206, http://dx.doi.org/10.1016/j.ijheatmasstransfer.2012.03.060.

[23] M.C. Coolen, R.N. Kieft, C.C. Rindt, A.A. Van Steenhoven, Application of 2-D LIF temperature measurements in water using a Nd:YAG laser, Exp. Fluids (ISSN: 07234864) 27 (5) (1999) 420–426, http://dx.doi.org/10.1007/s003480050367.

[24] P. Lavieille, F. Lemoine, G. Lavergne, M. Lebouché, Evaporating and combusting droplet temperature measurements using two-color laser-induced fluorescence, Exp. Fluids (ISSN: 07234864) 31 (1) (2001) 45–55, http://dx.doi.org/10.1007/s003480000257.

[25] J. Sakakibara, K. Hishida, M. Maeda, Vortex structure and heat transfer in the stagnation region of an impinging plane jet (simultaneous measurements of velocity and temperature fields by digital particle image velocimetry and laser-induced fluorescence), Int. J. Heat Mass Transfer (ISSN: 00179310) 40 (13) (1997) 3163–3176, http://dx.doi.org/10.1016/S0017-9310(96)00367-5.

[26] K. Hishida, J. Sakakibara, Combined planar laser-induced fluorescence-particle image velocimetry technique for velocity and temperature fields, Exp. Fluids (ISSN: 07234864) 29 (SUPPL. 1) (2000) http://dx.doi.org/10.1007/s003480070015.

[27] A.S. Nebuchinov, Y.A. Lozhkin, A.V. Bilsky, D.M. Markovich, Combination of PIV and PLIF methods to study convective heat transfer in an impinging jet, Exp. Therm Fluid Sci. (ISSN: 08941777) 80 (2017) 139–146, http://dx.doi.org/10.1016/j.expthermflusci.2016.08.009.

[28] J. Sakakibara, R.J. Adrian, Measurement of temperature field of a Rayleigh-Bénard convection using two-color laser-induced fluorescence, Exp. Fluids (ISSN: 07234864) 37 (3) (2004) 331–340, http://dx.doi.org/10.1007/s00348-004-0821-3.

[29] H.J. Seuntiëns, R.N. Kieft, C.C.M. Rindt, A.A. Van Steenhoven, 2D temperature measurements in the wake of a heated cylinder using LIF, Exp. Fluids (ISSN: 07234864) 31 (5) (2001) 588–595, http://dx.doi.org/10.1007/s003480100338.

[30] A. Charogiannis, J. Sik An, V. Voulgaropoulos, C.N. Markides, Structured planar laser-induced fluorescence (S-PLIF) for the accurate identification of interfaces in multiphase flows, Int. J. Multiph. Flow (ISSN: 03019322) 118 (2019) 193–204, http://dx.doi.org/10.1016/j.ijmultiphaseflow.2019.06.002.

[31] M. Stiti, A. Labergue, F. Lemoine, S. Leclerc, D. Stemmelen, Temperature measurement and state determination of supercooled droplets using laser-induced fluorescence, Exp. Fluids (ISSN: 07234864) 60 (4) (2019) 1–13, http://dx.doi.org/10.1007/s00348-018-2672-3.

[32] J.M. Savino, Experimental and analytical study of the transient solidification of a warm liquid flowing over a chilled flat plate, Technical report, National Aeronautics and Space Administration, 1967.

[33] B.J. Kaaks, M. Rohde, J.-l. Kloosterman, D. Lathouwers, An energy-conservative DG-FEM approach for solid–liquid phase change, Numer. Heat Transfer B (ISSN: 1040-7790) (2023) 1–27, http://dx.doi.org/10.1080/10407790.2023.2211231, URL https://www.tandfonline.com/doi/full/10.1080/10407790.2023.2211231.

[34] L.K. Hjertager, B.H. Hjertager, N.G. Deen, T. Solberg, Measurement of turbulent mixing in a confined wake flow using combined PIV and PLIF, Canad. J. Chem. Eng. (ISSN: 00084034) 81 (6) (2003) 1149–1158, http://dx.doi.org/10.1002/cjce.5450810604.

[35] M.M. Breunig, H.P. Kriegel, R.T. Ng, J. Sander, LOF: Identifying density-based local outliers, in: SIGMOD 2000 - Proceedings of the 2000 ACM SIGMOD International Conference on Management of Data, 2000, pp. 93–104, http://dx.doi.org/10.1145/342009.335388.

[36] P.T. Boggs, J.E. Rogers, Orthogonal distance regression, Contemp. Math. 112 (1990) 183–194, http://dx.doi.org/10.1090/conm/112/1087109.

[37] J.C. Mulligan, D.D. Jones, Experiments on heat transfer and pressure drop in a horizontal tube with internal solidification, Int. J. Heat Mass Transfer (ISSN: 00179310) 19 (2) (1976) 213–219, http://dx.doi.org/10.1016/0017-9310(76)90115-0.